

High-order h-adaptive discontinuous Galerkin methods for ocean modeling

P. E. Bernard¹, N. Chevaugnon³, V. Legat¹, E. Deleersnijder^{2,1}, J.-F. Remacle^{1,3}

¹ Center for Systems Engineering and Applied Mechanics (CESAME), Université catholique de Louvain, B-1348 Louvain-la-Neuve, Belgium.

² Institut d'astronomie et de géophysique G. Lemaître, Université catholique de Louvain, B-1348 Louvain-la-Neuve, Belgium.

³ Département d'Architecture, d'Urbanisme de Génie Civil et Environnemental, Université catholique de Louvain, B-1348 Louvain-la-Neuve, Belgium.

Accepted for publication in Ocean Dynamics, 6 november 2006.

the date of receipt and acceptance should be inserted later

Key words. Shallow Water Equations, h-Adaptivity, discontinuous Galerkin, a posteriori error estimation

Abstract. In this paper, we present an h-adaptive discontinuous Galerkin formulation of the shallow water equations. For a discontinuous Galerkin scheme using polynomials up to order p , the spatial error of discretization of the method can be shown to be of the order of h^{p+1} , where h is the mesh spacing. It can be shown by rigorous error analysis that the discontinuous Galerkin method discretization error can be related to the amplitude of the inter-element jumps. Therefore we use the information contained in jumps to build error metrics and size field. Results are presented for ocean modeling problems. A first experiment shows that the theoretical convergence rate is reached with the discontinuous Galerkin high-order h-adaptive method applied to the Stommel wind-driven gyre. A second experiment shows the propagation of an anticyclonic eddy in the Gulf of Mexico.

1 Introduction

The discontinuous Galerkin (DG) method has become a very attractive method especially for advection-dominated problems (e.g. CKS00; ADFK02; BR97). The main advantage is its flexibility in terms of mesh and shape functions. Moreover, the compactness of the stencil is maintained for high order efficient parallel implementation. Recent advances coming from the integration-free version of the formulation (e.g. LA99; AS98) allow for an enhancement of the computational efficiency of the DG method. The quadrature free implementation is especially useful at high polynomials orders.

In our work, we aim to develop a global ocean circulation model where the geometry is complex enough to justify the

shift from traditional structured grids models to unstructured meshes (e.g. HRLD04; PDE05). In ocean modeling, important dynamics features like meso-scale eddies have to be followed in time and solved accurately. The ocean exhibits many different length scales in time and space, with very unsteady behaviour and almost discontinuous fields. The meso-scale processes contain a huge part of the ocean energy and have to be captured. Dynamic mesh adaptation strategies following those structures represent a great potential in the field of ocean modeling (e.g. Beh98; HH02; NTL05; GHW02). In this framework of a new unstructured ocean model, we believe that the DG method is a good candidate because it provides a simple and efficient error estimator for any order p , which means a simple and efficient way to deal with mesh adaptivity. Moreover, the DG method ensures local conservation which may be a critical issue in ocean modeling, and is particularly efficient for advection-dominated problems.

Recent applications (e.g. Bak97; SB97; GBL02; CXH⁺05) show that transient mesh adaptation technologies are mature enough to tackle difficult problems. The computational overhead of modifying the mesh is negligible compared to the overall gain in computation time and accuracy.

Starting from a fast implementation of the DG method, originally developed to solve wave propagation problems (e.g. CRG⁺05), we first discuss the implementation of the shallow water equations, in particular the choice of an appropriate Riemann solver. After a brief description of the mesh-adaptation package, *MeshAdapt* developed at SCOREC¹ (e.g. RLSF05; Li03), we detail the mesh adaptation strategy based

¹ SCOREC, Scientific Computation Research Center, Rensselaer Polytechnic Institute, Troy, NY, USA

on the error estimation for the DG method. We then provide some preliminary validations of the method by solving the classical Stommel model, before turning to an idealized simulation of an anticyclonic baroclinic eddy in the Gulf of Mexico.

2 Discontinuous Galerkin Method for shallow water equations

It is only recently that the DG method has been applied to the shallow water equations (e.g. SK00; DP02; DP04; NTL05; GHW02). These equations have been used for many years for solving a variety of problems, such as atmospheric, oceanic, dam breaking (e.g. SZ02a; RSL06) or river flow problems (e.g. Vre94).

2.1 Shallow water equations

The shallow water equations describe the flow of a thin layer of incompressible fluid, with no stratification, under the influence of a gravitational force. This model is based on the assumption that the vertical dimension is very small compared to the horizontal one. A vertical integration over the depth of the fluid layer $H(\mathbf{x}, t) = h(\mathbf{x}) + \eta(\mathbf{x}, t)$ (where h is the unperturbed height of the water column and η the surface elevation measured from a reference height (Figure (1))) is then performed on the 3D Navier-Stokes equations. The bottom and the surface of the ocean are impermeable, which yields the two boundary conditions required for integration.

The two-dimensional, conservative form of the shallow water equations is then obtained, not in terms of pressure and velocity, but in terms of water depth and mean velocity:

$$\frac{\partial H}{\partial t} + \nabla \cdot (H\mathbf{v}) = 0, \quad (1)$$

$$\frac{\partial H\mathbf{v}}{\partial t} + \nabla \cdot (H\mathbf{v}\mathbf{v}) + gH\nabla\eta + f\mathbf{e}_z \times H\mathbf{v} = \frac{\boldsymbol{\tau}^s - \boldsymbol{\tau}^b}{\rho}, \quad (2)$$

where t is time, f is the Coriolis parameter, \mathbf{v} is the depth-averaged horizontal velocity, g is the gravitational acceleration, $\boldsymbol{\tau}^s$ and $\boldsymbol{\tau}^b$ denote the surface and bottom stresses, respectively.

The main parameters are

- the Rossby number: $Ro = \frac{U}{L_f}$, with U a characteristic velocity and L a characteristic length. The Rossby number is the ratio between the Earth period and the flow period. It represents the relative importance of the Coriolis effect.
- the Froude number: $Fr = \frac{U}{c}$, with c the speed of the gravity waves. The Froude number represents the ratio between the flow velocity and the gravity waves velocity.

It is similar to the Mach number in compressible fluid dynamics problems. The flow is said to be critical when the Froude number reaches $Fr = 1$.

The free surface allows propagation of gravity waves at speed $c = \sqrt{gH}$ (those are equivalent to sound waves in Euler equations). In the case of an ocean modeling problem, the speed of gravity waves is typically one hundred to one thousand times faster than the speed of the fluid itself.

2.2 Discontinuous Galerkin Method applied to shallow water equations

We consider a closed two dimensional domain Ω . Its boundary $\partial\Omega$ has a normal \mathbf{n} defined everywhere. We seek to determine the vector of unknowns $\mathbf{U}(\Omega, t)$ as the solution of a system of conservation laws:

$$\frac{\partial \mathbf{U}}{\partial t} + \nabla \cdot \mathbf{F}(\mathbf{U}) = \mathbf{S}, \quad (3)$$

where \mathbf{F} is the flux matrix and \mathbf{S} is the vector containing the source terms.

We multiply (3) by a test function \mathbf{w} and integrate on the domain Ω to obtain this classical weak formulation:

$$\langle \partial_t \mathbf{U}, \mathbf{w} \rangle_\Omega + \langle \nabla \cdot \mathbf{F}(\mathbf{U}), \mathbf{w} \rangle_\Omega = \langle \mathbf{S}, \mathbf{w} \rangle_\Omega, \quad (4)$$

with the scalar product: $\langle a, b \rangle_v = \int_v ab \, dv$.

The computational domain is divided into a set of elements Ω_e called a mesh. In the case of a DG method, we approximate the unknown fields using piecewise discontinuous polynomial approximations: in element Ω_e , the fields \mathbf{U} are approximated using p -order polynomials in each element with no inter element continuity requirements. The total number of degrees of freedom for a fully triangular mesh of N elements is therefore equal to $N \times [(p+1)(p+2)/2] \times m$, with m the number of unknown fields, i.e. three in the shallow water case. Because all approximations are disconnected, the weak form (4) can be written in each element. After having integrated the divergence of fluxes by parts in (4), we obtain

$$\langle \partial_t \mathbf{U}, \mathbf{w} \rangle_{\Omega_e} - \langle \mathbf{F}(\mathbf{U}), \nabla \mathbf{w} \rangle_{\Omega_e} + \langle \mathbf{F}(\mathbf{U}) \cdot \mathbf{n}, \mathbf{w} \rangle_{\partial\Omega_e} = \langle \mathbf{S}, \mathbf{w} \rangle_{\Omega_e}. \quad (5)$$

A numerical flux function has to be supplied to the formulation because unknowns \mathbf{U} are multiply valued at element interfaces $\partial\Omega_e$.

Two neighboring elements in continuous FEM share common nodes that ensure the continuity of the finite element approximation. With the DG method, fields are discontinuous through element edges. Jumps at element interfaces have to be controlled by a numerical flux function. In this paper, we consider triangular meshes exclusively. The boundary $\partial\Omega_e$ of a triangle Ω_e is composed of three edges $\partial\Omega_{e_k}$, $k = 1, \dots, 3$.

The flux function is computed on those three edges using a combination of the fields on both sides of the edge, i.e. using the unknown fields \mathbf{U} inside element Ω_e and using the unknown fields \mathbf{U}^k in the neighboring triangle across edge $\partial\Omega_{e_k}$. We have:

$$\langle \mathbf{F}(\mathbf{U}) \cdot \mathbf{n}, \mathbf{w} \rangle_{\partial\Omega_e} = \sum_{k=1}^3 \langle \mathbf{F}_n(\mathbf{U}, \mathbf{U}^k), \mathbf{w} \rangle_{\partial\Omega_{e_k}}.$$

The centered DG scheme uses the average of fluxes as the flux function:

$$\mathbf{F}_n(\mathbf{U}, \mathbf{U}^k) = \frac{1}{2} (\mathbf{F}(\mathbf{U}) + \mathbf{F}(\mathbf{U}^k)) \cdot \mathbf{n}.$$

Though producing no spatial dissipation, the use of a centered scheme may cause advective instabilities when the discretization is unable to resolve a certain range of wave numbers (e.g. CRG⁺05). Riemann solvers are the extension of upwind schemes to non-linear systems of conservation laws.

The idea of the Riemann solver consists in upwinding the characteristics variables. The projection of (3) without source terms on the normal direction \mathbf{n} is written as:

$$\frac{\partial \mathbf{U}}{\partial t} + \frac{\partial \mathbf{F}_n(\mathbf{U})}{\partial n} = \frac{\partial \mathbf{U}}{\partial t} + \mathbf{A}_n \frac{\partial \mathbf{U}}{\partial n} = 0, \quad (6)$$

where $\mathbf{A}_n = \frac{\partial \mathbf{F}_n}{\partial \mathbf{U}}$ is the jacobian matrix of the flux vector in the normal direction \mathbf{F}_n . This jacobian matrix can be written as $\mathbf{A}_n = \mathbf{R}\mathbf{\Lambda}\mathbf{R}^{-1}$ with matrices of eigenvectors \mathbf{R} and eigenvalues $\mathbf{\Lambda}$. We can then derive the following one-dimensional transport equation:

$$\frac{\partial \mathbf{U}^*}{\partial t} + \mathbf{\Lambda} \frac{\partial \mathbf{U}^*}{\partial x} = 0. \quad (7)$$

The characteristics variables $\mathbf{U}^* = \mathbf{R}^{-1}\mathbf{U}$, the *Riemann invariants*, are convected along the normal direction to the edge of the element. The transport velocities are the eigenvalues of the problem which are used to choose the appropriate values on the edge. More precisely, upwinding can be applied on the characteristics variables convected across the edge. Note that the source terms \mathbf{S} are not taken into account in equation (6) since they have no influence on the Riemann invariants or on the sign of the eigenvalues neither. Note also that no diffusion term was considered, since the Riemann solver only deals with advection. This diffusion term can be solved in the usual way with an integration by part and a centered scheme to define the interface values.

It has been shown that this Riemann solver introduces the minimum numerical dissipation required to stabilize the numerical scheme in the presence of transport terms.

The shallow water equations lead to the following expressions for \mathbf{U} and \mathbf{F} :

$$\mathbf{U} = \begin{bmatrix} H \\ Hu \\ Hv \end{bmatrix}, \quad \mathbf{F}(\mathbf{U}) = \begin{bmatrix} Hu & Hv \\ Huv + g\frac{H^2}{2} & Huv \\ Hvu & Hvv + g\frac{H^2}{2} \end{bmatrix}.$$

The eigenvalues matrix read:

$$\mathbf{\Lambda} = \begin{bmatrix} \mathbf{v} \cdot \mathbf{n} + c & 0 & 0 \\ 0 & \mathbf{v} \cdot \mathbf{n} - c & 0 \\ 0 & 0 & \mathbf{v} \cdot \mathbf{n} \end{bmatrix},$$

where $c = \sqrt{gh}$ is the gravity waves velocity.

In order to keep the same general formulation (3), the transport terms require the use of the conservative formulation. Advection terms are thus expressed as a divergence $\nabla \cdot (H\mathbf{v}\mathbf{v})$. This conservative form is non linear, even without transport terms, because of the presence of the elevation term $\nabla \cdot \left(\frac{H^2}{2}\right)$. But the transport terms lead to a complex and computationally prohibitive exact Riemann solver. Approximate Riemann solvers are proved to produce more numerical dissipation than the exact solver, but numerical experience suggests that this choice does not have a significant impact on the accuracy of the solution, especially when polynomial degree increases. The conservative formulation can thus be solved with, for example, a Roe solver, which consists of the exact solution to a linearized Riemann problem, and is consistent with the discrete entropy condition (e.g. Roe81). The basic idea consists in considering that over a small time step, the characteristics curves propagating information can be replaced by straight lines. This approximation leads to consider as constant the eigenvalues and eigenvectors matrices $\mathbf{\Lambda}$ and \mathbf{R} .

The Roe numerical flux for shallow water equations (e.g. RSL06; SZ02b) can be written as:

$$\begin{aligned} \mathbf{F}_n(\mathbf{U}, \mathbf{U}^k) = & \frac{1}{2} [\mathbf{F}(\mathbf{U}) + \mathbf{F}(\mathbf{U}^k)] \cdot \mathbf{n} + \\ & \frac{1}{2} Fr [\mathbf{F}(\mathbf{U}) - \mathbf{F}(\mathbf{U}^k)] \cdot \mathbf{n} + \\ & \frac{1}{2} c_A (1 - Fr^2) [\mathbf{U} - \mathbf{U}^k]. \end{aligned} \quad (8)$$

The first term corresponds to the centered flux, the others are dissipation terms. The average Froude number Fr is defined as:

$$Fr = \frac{\mathbf{v}_A \cdot \mathbf{n}}{c_A}, \quad (9)$$

with \mathbf{v}_A a Roe-averaged velocity and c_A a Roe-averaged wave speed that are computed as

$$\begin{aligned} u_A &= \frac{u\sqrt{h} + u^k\sqrt{h^k}}{\sqrt{h} + \sqrt{h^k}}, \\ v_A &= \frac{v\sqrt{h} + v^k\sqrt{h^k}}{\sqrt{h} + \sqrt{h^k}}, \\ c_A &= \sqrt{g\frac{h + h^k}{2}}. \end{aligned}$$

3 Mesh-adaptation

Efforts on the development of mesh adaptation techniques have been underway for over twenty years and have provided a number of important theoretical and practical results (e.g. RLSF05; Bak97; SB97; GBL02).

It is only recently that mesh adaptation has been applied to transient flow problems and in particular to ocean applications (e.g. PPG⁺05). It has been shown that DG techniques allow to control the quality of a solution transfer between two consecutive adaptive meshes (e.g. RLSF05). It is indeed possible to adapt the mesh very often and project solutions without alteration.

We have recently developed mesh adaptation algorithms that allow to locally modify a given 2D or 3D mesh in order to make it conform to a given size field (e.g. RLSF05; Li03; LRCS04). The *MeshAdapt* software package performs local mesh modifications, essentially edge swaps, edge collapses and edge splits. Note that we use here only a small set of the package capabilities: *MeshAdapt* is able to perform 3D anisotropic mesh adaptation in parallel.

It is obvious that an anisotropic mesh is the optimal choice, especially where the flow is itself anisotropic (e.g. RLSF05). But in this framework of a first experiment in coupling ocean modeling and mesh adaptation, only isotropic meshes were considered in order to simplify the mesh metric definition.

3.1 Description of the MeshAdapt package

A mesh metric field is a smooth positive function $\mathcal{M}(x, y)$ defined over the domain Ω . The length of a mesh edge e is computed as $l_e = \int_e \sqrt{\mathcal{M}(x, y)} dl$. The aim of the mesh adaptation procedure is to modify an existing mesh to make it a unit mesh, i.e. a mesh for which every edge is of size $l_e = 1$. At one given time step, a metric field is computed at every node of the mesh using the results of an a posteriori error estimation procedure. The mesh adaptation algorithm then modifies locally the present mesh by:

- Splitting all the long edges,
- Collapsing all the short edges.

Edge swaps are also performed in order to optimize the quality of the resulting mesh. The mesh adaptation procedure is applied iteratively until a convergence criterion is satisfied. The different local mesh modifications used here are depicted in Figure 2.

Typically, the algorithm stops when every edge of the domain has a dimensionless size in the interval $l_e \in [0.5; 1.4]$. A long edge is an edge such that $l_e > 1.4$ and a short edge is an edge of size $l_e < 0.5$. Using this interval for short and long edges ensures that the two new edges created by a bisection will not be short edges. Oscillations between refinements and coarsenings are therefore prevented. More details about this mesh adaptation procedure can be found in previous papers (e.g. RLSF05; Li03; LRCS04).

As an example, we see on Figure 3 two mesh size fields together with the respective adaptive meshes. Those results come out of a simulation that will be described below in more details. Both plots on top of Figure 3 were computed at an early stage of the simulation while the bottom plots are the result of about 100 adaptations.

3.2 Error estimation

Here, we only consider the spatial error of discretization. Note that it has been shown (e.g. CHG⁺05) that, using an explicit Runge-Kutta time stepping of order $p + 1$ in time together with a DG method of order p in space, the spatial error is at least one order of magnitude higher than the error in time.

The approximated fields in a DG method are discontinuous at inter-element boundaries. It has been shown (e.g. MCR05) that the inter-element jumps of the solution are converging at the same rate as the discretization error. If we consider the situation depicted at Figure 4, the jump at one point \mathbf{p}_k of edge $\partial\Omega_{e_k}$ converges at the same rate as the DG error:

$$[\mathbf{U} - \mathbf{U}^k](\mathbf{p}_k) = \mathcal{O}(h^{p+1}),$$

where h is the local mesh size. Notice that h always denotes the local mesh size in the following section.

It has been shown that the DG solution was superconvergent at downwind faces (e.g. MCR05). This means that, on $\partial\Omega_{e_k}$, either \mathbf{U} or \mathbf{U}^k is a good approximation (at order h^{2p+1}) of the exact solution. Here, we choose the average value to be the approximation of the exact solution \mathbf{U}_{ex} :

$$\mathbf{U}_{ex}(\mathbf{p}_k) \simeq \frac{1}{2} [\mathbf{U} + \mathbf{U}^k](\mathbf{p}_k).$$

We have then:

$$\mathbf{E}(\mathbf{p}_k) = [\mathbf{U} - \mathbf{U}_{ex}](\mathbf{p}_k) \simeq \frac{1}{2} [\mathbf{U} - \mathbf{U}^k](\mathbf{p}_k).$$

The jumps are therefore a good image of the discretization error and can be used as an error indicator. Here, we show that, using an appropriate measure of the jumps, we are able to use the jumps as an error estimator. We will compute local and global effectivity indices and show that they are optimal. We consider an average error along each edge.

$$\begin{aligned} \mathbf{e}_{\partial\Omega_{e_k}}^2 &= \frac{1}{|\partial\Omega_{e_k}|} \int_{\partial\Omega_{e_k}} \mathbf{E}^2 ds \simeq \frac{1}{4} \frac{1}{|\partial\Omega_{e_k}|} \int_{\partial\Omega_{e_k}} [\mathbf{U} - \mathbf{U}^k]^2 ds, \\ \mathbf{e}_{\partial\Omega_{e_k}} &= \mathcal{O}(h^{p+1}). \end{aligned}$$

For each element Ω_e , we compute an a posteriori error estimator by the following rule:

$$\mathbf{e}_{\Omega_e}^2 = \frac{1}{3} |\Omega_e| \sum_{k=1}^3 \mathbf{e}_{\partial\Omega_{e_k}}^2, \quad (10)$$

where $|\Omega_e|$ is the area of Ω_e . Note that the three mid-edge points of the triangle form a Gauss quadrature rule. Clearly, using this simple approach, the error is constant in one element and the resulting size field is still constant in each high order triangle. More complex rules can be computed for higher order polynomial approximations. The total error is calculated as the sum of all elementary errors

$$\mathbf{e}^2 = \int_{\Omega} \mathbf{E}^2 dv = \sum_e \mathbf{e}_{\Omega_e}^2. \quad (11)$$

The relative error is defined as:

$$\epsilon^2 = \frac{\int_{\Omega} \mathbf{E}^2 dv}{2 \int_{\Omega} \mathbf{U}^2 dv} = \frac{\mathbf{e}^2}{2 \|\mathbf{U}\|_{L^2}^2} = \mathcal{O}(h^{p+1}) \quad (12)$$

implying that it is smaller than 1. We define the local relative error as:

$$\epsilon_{\Omega_e}^2 = \frac{\mathbf{e}_{\Omega_e}^2}{2 \|\mathbf{U}\|_{L^2}^2}, \quad \text{with} \quad \sum_e \epsilon_{\Omega_e}^2 = \epsilon^2.$$

Our aim could be either to control the discretization error with a minimum number of elements or to control the number of elements in the optimal mesh while minimizing the discretization error.

Let us consider Ω_e an element of the initial mesh for which we have computed an error of ϵ_{Ω_e} . We know that, if h_e is the size of Ω_e (its circumscribed radius for example) and if h_e^* is the size of the elements of the optimal mesh on the region covered by Ω_e , we have:

$$\frac{\epsilon_{\Omega_e}}{\epsilon_{\Omega_e}^*} = \left(\frac{h_e}{h_e^*} \right)^{p+1}. \quad (13)$$

where $\epsilon_{\Omega_e}^*$ is the relative error defined in the region enclosed by Ω_e in the optimal mesh. The total error in the optimal mesh is then:

$$\epsilon^{*2} = \sum_e \epsilon_{\Omega_e}^{*2} = \sum_e \epsilon_{\Omega_e}^2 \left(\frac{h_e^*}{h_e} \right)^{2(p+1)} = \sum_e \epsilon_{\Omega_e}^2 r_e^{-2(p+1)}, \quad (14)$$

where r_e is a factor that represents the reduction of element sizes in element Ω_e . The number of elements N^* in the optimal mesh can be computed using the r_e 's. Clearly,

$$N^* = \sum_e r_e^d,$$

where d is the dimension of the problem. Here $d = 2$. The problem is either to minimize N^* while controlling $\epsilon^* = \bar{\epsilon}$ or to minimize ϵ^* while controlling $N^* = \bar{N}$. The first problem leads to the following saddle point optimization problem:

$$\min_{r_e} \max_{\lambda} \sum_e r_e^2 + \lambda \left(\sum_e \epsilon_{\Omega_e}^2 r_e^{-2(p+1)} - \bar{\epsilon}^2 \right),$$

where λ is a Lagrange multiplier. We find easily that:

$$r_e^2 = (\lambda(p+1)\epsilon_{\Omega_e}^2)^{1/(p+2)}. \quad (15)$$

The solution of the problem can be computed in a closed form if p is constant:

$$r_e = \bar{\epsilon}^{1/(p+1)} \epsilon_{\Omega_e}^{-1/(p+2)} \left[\sum_e \epsilon_{\Omega_e}^{2/(p+2)} \right]^{-1/(2p+2)}. \quad (16)$$

The second problem leads to:

$$\min_{r_e} \max_{\lambda} \sum_e \epsilon_{\Omega_e}^2 r_e^{-2(p+1)} + \lambda \left(\sum_e r_e^2 - \bar{N}^* \right),$$

where λ is another Lagrange multiplier. The solution is, for p constant:

$$r_e = \sqrt{\bar{N}^*} \epsilon_{\Omega_e}^{1/(p+2)} \left[\sum_e \epsilon_{\Omega_e}^{2/(p+2)} \right]^{-1/2}.$$

The r_e 's define the size field used to build the adapted mesh by means of local mesh modifications.

3.3 Projection of the solution

Once the mesh has been adapted, the solution on the previous mesh is projected on the adapted one. This is done by means of an L^2 projection. The DG method allows this projection to be done element by element. Another advantage of the DG method is that, during the edge split operation, the projection is exact and no error is introduced. The edge collapse operator is only used in regions of the domain where the error is low, so no significant error is introduced with this coarsening operation. Finally, the introduction of numerical diffusion is only expected when the swapping operation is applied. It is recommended to use an accurate integration scheme in the L^2 projection: the solution may be discontinuous across the edge that is swapped. Here, we do not consider node repositioning, typically Laplacian smoothing, because this mesh modification pattern introduces an excessive amount of numerical dissipation.

4 Application to Ocean modeling

In this section, we first perform a validation step on a benchmark problem: the Stommel model. An adaptive convergence experiment is performed in order to test both the convergent behavior of the DG scheme and the efficiency of the adaptive strategy. In a second experiment, we simulate the propagation of a typical anticyclonic baroclinic eddy in the realistic domain of the Gulf of Mexico.

4.1 Adaptive convergence applied to the Stommel gyre

Interesting simplifications can be done to the shallow water equations in order to obtain the Stommel model, used to perform the following convergence study.

First, the non linear transport terms $\nabla \cdot (H\mathbf{v}\mathbf{v})$ are neglected. Then we assume a constant bathymetry and the β -plane approximation, according to which the Coriolis parameter is a linear function of one space coordinate, i.e. $f = f_0 + \beta_0 y$, where $f_0 \approx 10^{-4} \text{ s}^{-1}$ and $\beta_0 \approx 10^{-11} \text{ m}^{-1} \text{ s}^{-1}$ are constants. The dissipation term is parametrized as $\tau^b = \gamma H\mathbf{v}$ where γ is a constant friction coefficient. The typical surface stress is given by $\tau^s = \tau_0 \sin(\pi y')$ with $y' = \frac{y}{L_y} \in [-0.5; 0.5]$ the non-dimensional coordinate with L_y the typical size of the domain along the y -dimension. Finally, the relative elevation is neglected compared to the bathymetry, leading to the following classical linearization: $H = h + \eta \cong h$. With those approximations, the linearized form of the shallow water equations becomes:

$$\frac{\partial \eta}{\partial t} + \nabla \cdot (h\mathbf{v}) = 0, \quad (17)$$

$$\frac{\partial \mathbf{v}}{\partial t} + g\nabla \eta + (f_0 + \beta_0 y)\mathbf{e}_z \times \mathbf{v} = -\gamma\mathbf{v} + \frac{\tau^s}{h\rho}. \quad (18)$$

Equations (17) and (18) are sometimes called the Stommel model which leads to the typical ‘‘Stommel gyre’’ (Figure(5)) (e.g. Sto48).

The Stommel equations are solved on a square of one thousand kilometers of side, and compared to the analytical solution. The Coriolis effect leads to a geostrophic balance, creating a recirculation cell. The linear part βy of the Coriolis factor f tends to move the eddy westward (for the northern hemisphere parameters), leading to a boundary layer at the western boundary of the domain. The size of this boundary layer is determined by the ratio $\frac{\gamma}{\beta L_x}$. The adaptive method is therefore very useful in order to capture the large gradients on this western boundary, while the eastern part of the domain does not require such a fine discretization. The analytical solution can be found in appendix A. On Figure (5), the typical Stommel stream function is shown with its western boundary layer.

Two different polynomial orders (P1 and P4 elements) have been used, giving two different theoretical convergence rates, according to h_e^{p+1} from relation (13) where h_e is the local element size.

Figure (6.a) presents the evolution of the L^2 error norm with the characteristic element size on uniformly refined meshes. The numerical results show that the theoretical asymptotic behaviour is only attained using dense uniform meshes.

The Figure (6.b) presents the evolution of the L^2 norm of the error versus the characteristic size of the elements cor-

responding to a given target error. The numerical results are compared to the theoretical convergence rates lines.

Numerical results fit the theoretical rates, both with fixed regular mesh and adapted mesh. A kind of oscillatory behaviour is still present on the adaptive mesh which can be explained with the use of the interval $[0.5; 1.4]$ to transform the error estimation into a new edge size field, as discussed in the previous paragraph. To reach the same error norm of approximately 5×10^{-3} with linear shape functions, the non-adaptive structured regular mesh required 648 elements while the adaptive method needs only 79 elements. On the same mesh, the error is more than a hundred times smaller with P4 element than with P1.

For the same convergence experiment, we plot the maximum error compared to the degrees of freedom. As we see on Figure 7-(a), for the same maximum error of 10^{-2} , the adaptive strategy with first order elements leads to use five times less degrees of freedom. And with the use of fourth order elements, we obtain about one hundred less degrees of freedom for this same maximum error. The meshes on Figures 7-(b) and 7-(c) are respectively those obtained with the first and fourth order adaptive meshes.

Finally, a classical way to quantify the quality of an error estimator is the effectivity index (e.g. Ain04), defined as the ratio between the norm of the error estimator ϵ and the norm of the exact error e . The global index is:

$$\theta = \frac{\|\epsilon\|_{\mathcal{L}_2}}{\|e\|_{\mathcal{L}_2}}, \quad (19)$$

while the local one is defined in the same way on each element. With the first order elements, mean jumps have been defined on each node as the mean of the jumps on adjacent elements to compute the norm $\|\epsilon\|_{\mathcal{L}_2}$. Figure (8) shows the evolution of this index with the number of elements. The local index on this figure is defined as the simple mean of locals indexes on the whole domain. The global index tends to a value of 1.03. A value so close to one indicates that the jumps seem to be relevant as error estimator. The local effectivity field is depicted on Figure (9).

Our choice of mesh size field based on the only interface element jump leads to the right convergence rate, regardless of polynomial order. Adaptivity and the use of high order elements both seem useful, but combining the two seems particularly efficient and simple with the DG method.

4.2 Propagation of a baroclinic anticyclonic eddy at midlatitudes

The following results concern the propagation of a typical baroclinic anticyclonic eddy at midlatitudes (e.g. HRLD05) in the Gulf of Mexico. The basin is assumed closed, the

Yucatan Channel and the Florida Straits with their inflow and outflow are ignored. Although this experiment is highly idealized, it is expected to represent some of the features of the life cycle of anticyclonic eddies with the adaptive capture of eddies propagation.

To model the flow in the Gulf of Mexico, it is essential to take into account its baroclinic aspects. In this respect, the simplest approach consists in assuming that the domain is divided into two constant density layers separated by a free, impermeable interface: the pycnocline. As the lower layer is much deeper than the top layer, it is possible to further simplify the model to a reduced-gravity one. Such a model is widely used in oceanography and limnology (e.g. NDP03; LO85; WLO89; BO80). To establish reduced-gravity equations, a closure hypothesis on the pressure force is needed, that eventually leads to a closed set of equations governing the motion in the surface layer. Accordingly, the downward displacement of the pycnocline, ξ , and the depth-averaged velocity in the surface layer, \mathbf{v} , obey equations that are similar to the classical shallow-water equations introduced in section 2:

$$\frac{\partial \xi}{\partial t} + \nabla \cdot (H\mathbf{v}) = 0, \quad (20)$$

$$\frac{\partial H\mathbf{v}}{\partial t} + \nabla \cdot (H\mathbf{v}\mathbf{v}) + f\mathbf{e}_z \times \mathbf{v} = -g'H\nabla\xi, \quad (21)$$

where $H = h + \xi$ is the actual depth of the upper layer (Figure(10)), given that h is the unperturbed equilibrium height of the surface layer; g' is the so-called reduced gravity. The latter is defined as $g' = g\delta$, with g the gravity and $\delta = \frac{\Delta\rho}{\rho}$ the relative density difference between the bottom and the surface layers.

A Gaussian distribution of water elevation η is assumed at initial time:

$$\eta(x, y, t = 0) = C \exp[-D(x^2 + y^2)], \quad (22)$$

with $C = 68.2 \text{ m}$ and $D = 5.92 \times 10^{-11} \text{ m}^{-2}$. The β -plane assumption is made (i.e. $f = f_0 + \beta y$) with the Coriolis parameters taken at $25N$: $f_0 \cong 6.1635 \times 10^{-5} \text{ s}^{-1}$ and $\beta_0 \cong 2.0746 \times 10^{-11} \text{ m}^{-1} \text{ s}^{-1}$. An initial velocity field is taken to be in geostrophic balance, which means:

$$u(\mathbf{x}, t = 0) = -\frac{g}{f} \frac{\partial \eta}{\partial y} = 2 \frac{g'}{f_0 + \beta_0 y} CDy \exp[-D(x^2 + y^2)],$$

$$v(\mathbf{x}, t = 0) = \frac{g}{f} \frac{\partial \eta}{\partial x} = -2 \frac{g'}{f_0 + \beta_0 y} CDx \exp[-D(x^2 + y^2)],$$

leading to a maximum initial flow speed of 1 ms^{-1} with $g' = 0.137 \text{ ms}^{-2}$ and $h = 100 \text{ m}$. The maximum Froude number reached during the simulation is $\max(Fr) = 0.5$, which is very high compared to the simple Stommel model, and the Rossby number is $Ro \cong 9 \times 10^{-3}$.

No wind forcing and no bottom friction is applied. The Coriolis effect is thus the only source term responsible for moving the eddy westward. This propagation of slow Rossby waves, represented with the shallow water equations, is due to the β -effect. Such waves have a major effect on the large scale circulation, and thus on weather and climate. For instance, Rossby waves can intensify western boundary currents, which transport huge quantities of heat. Even a minor shift in the position of the current can thus affect weather over large areas of the globe.

Figure (11) represents the evolution of the eddy with the Coriolis forcing. Its westward propagation is captured by the mesh evolution (right column): a minimum size field of ten kilometers has been applied to keep a low number of elements.

After one week of physical time simulation, the mesh has been adapted three times to capture the regions with larger variations: the eddy region, and the coast lines, where gravity waves come and bounce back. At this time, the mesh presents approximately 3000 elements. The eddy keeps moving westward until approximately week 11, when it reaches the coast. Then, its shape is modified when a second eddy appears, spinning in the opposite direction. The number of elements grows up to 7000 in order to fit this large variation region. On week 14, one can see the slow creation of a western boundary current, flowing southward. As the eddy keeps moving southward, the mesh seems to perfectly capture the evolution of this current and the eddy generated at the southern extremity of the golf on week 23. The initial eddy then collapses to generate smaller eddies which keep spinning and mixing on the western boundary. The number of elements decreases then to the initial value of approximately 3000.

The mesh has been well adapted to eddies and currents, but large field variations and mesh refinement must also be noticed on sharp and non regular coasts, as on the north and east-north of the Gulf. A restriction of ten kilometers has been applied on the size of elements on adaptive mesh. To reach the same size with a non-adaptive mesh, about 34000 elements would be required with the first order polynomial shape functions.

5 Conclusion

In this paper we show that both high-order elements and mesh adaptivity, coupled with discontinuous Galerkin method, can be a very attractive approach to simulate ocean flows. The DG method provides a simple and efficient way to deal with those two techniques, by providing an efficient error estimator. This DG method has been successfully applied to the shallow water equations, and seems to be particularly promising in this framework of a new ocean model.

Of course, in terms of the physic that need to be modeled, lots of work need to be done in code implementation in order to compare with established ocean model. Our next step toward this goal will be the ability to deal with realistic bathymetry. On the mesh adaptation side of the work, we plan to take full advantage of the anisotropic mesh adaptation features of the *MeshAdapt* package.

Acknowledgements

Eric Deleersnijder is a Research associate with the Belgian National Fund for Scientific Research (FNRS). The present study was carried out within the scope of the project ‘‘A second-generation model of the ocean system’’, which is funded by the *Communaut  Francaise de Belgique*, as *Actions de Recherche Concert es*, under contract ARC 04/09-316. This work is a contribution to the SLIM² project. The authors gratefully acknowledge Emmanuel Hanert for the comments and help he provided during the preparation of this paper.

A Analytical solution of the Stommel problem

The analytical steady solution is given by :

$$\begin{aligned}\Psi(x, y) &= \frac{\mathcal{D}^3 \tau_0 L_y}{\pi^2 \gamma \rho} f_1(x) \cos(\pi y) \\ U(x, y) &= \frac{\mathcal{D} \tau_0}{\pi \gamma \rho} f_1(x) \sin(\pi y) \\ V(x, y) &= \frac{\mathcal{D} \tau_0}{\pi \gamma \rho \delta} f_2(x) \cos(\pi y) \\ \eta(x, y) &= \frac{\mathcal{D} \tau_0 f_0 L_x}{\pi \gamma \rho \delta g h} \left[-\frac{C_{drag}}{\delta \pi} f_2(x) \sin(\pi y) \right. \\ &\quad \left. + \frac{1}{\pi} f_1(x) \left(\cos(\pi y)(1 + \beta y) - \frac{\beta}{\pi} \sin(\pi y) \right) \right]\end{aligned}$$

with the following functions :

$$\begin{aligned}f_1(x) &= \frac{\pi}{\mathcal{D}} \left(1 + \frac{(e^{z^-} - 1)e^{z^+x} + (1 - e^{z^+})e^{z^-x}}{e^{z^+} - e^{z^-}} \right) \\ f_2(x) &= \frac{1}{\mathcal{D}} \frac{(e^{z^-} - 1)z_+ e^{z^+x} + (1 - e^{z^+})z_- e^{z^-x}}{e^{z^+} - e^{z^-}} \\ \mathcal{D} &= \frac{(e^{z^-} - 1)z_+ + (1 - e^{z^+})z_-}{e^{z^+} - e^{z^-}} \\ z_{\pm}^+ &= \frac{-1 \pm \sqrt{1 + (2\pi\delta\epsilon)^2}}{2\epsilon}\end{aligned}$$

The dimensionless parameters used are : the aspect ratio of the domain $\delta = \frac{L_x}{L_y}$, the ration between bottom friction and Coriolis effect $C_{drag} = \frac{\gamma}{f_0}$ and $\epsilon = \frac{\gamma}{L_x \beta_0}$ the parameter defining the boundary layer width.

² SLIM, Second-Generation Louvain-la-Neuve Ice-ocean Model, www.climate.be/SLIM

References

- Adjerid S, Devine KD, Flaherty JE, Krivodonova L (2002) A posteriori error estimation for discontinuous Galerkin solutions of hyperbolic problems. *Computer Methods in Applied Mechanics and Engineering*, 191:1097–1112.
- Ainsworth M (2004) Dispersive and dissipative behavior of high order Discontinuous Galerkin finite element methods. *Journal of Computational Physics*, 198(1):106–130.
- Atkins HL, Shu CW (1998) Quadrature-free implementation of discontinuous galerkin methods for hypebolic equations. *AIAA Journal*, 36(5).
- Baker TJ (1997) Mesh adaptation strategies for problems in fluid dynamics. *Finite Elem. Anal. Des.*, 25(3-4):243–273.
- Behrens J (1998) Atmospheric and ocean modeling with an adaptive finite element solver for the shallow-water equations. *Applied Numerical Mathematics*, 26:217–226.
- Busalacchi AJ, O’Brian JJ (1980) The seasonal variability in a model of the tropic pacific. *J. Phys. Oceanogr.*, 10:1929–1951.
- Bassi F, Rebay S (1997) A high-order accurate discontinuous finite element solution of the 2d Euler equations. *Journal of Computational Physics*, 138:251–285.
- Chevaugeron N, Hillewaert K, Gallez X, Ploumhans P, Remacle J-F (2005) Optimal numerical parameterization of discontinuous galerkin method applied to wave propagation problems. *Journal of Computational Physics*,. In press.
- Cockburn B, Karniadakis GE, Shu CW (2000) *Discontinuous galerkin Methods*. Lecture Notes in Computational Science and Engineering. Springer Verlag.
- Chevaugeron N, Remacle J-F, Gallez X, Ploumans P, Caro S (2005) Efficient discontinuous galerkin methods for solving acoustic problems. In 11th AIAA/CEAS Aeroacoustics Conference.
- Chevaugeron N, Xin J, Hu P, Li X, Cler D, Flahertyand JE, Shephard MS (2005) Discontinuous galerkin methods applied to shock and blast problems. *J. Sci. Comput.*, 22(1):227–243.
- Dawson C, Proft J (2002) Discontinuous and coupled continuous/discontinuous galerkin methods for the shallow water equations. *Computer Methods in Applied Mechanics and Engineering*, 191(41-42):4721–4746.
- Dawson C, Proft J (2004) Coupled discontinuous and continuous galerkin finite element methods for the depth-integrated shallow water equations. *Computer Methods in Applied Mechanics and Engineering*, 193(3-5).
- George PL, Borouchaki H, Laug P (2002) An efficient algorithm for 3d adaptive meshing. *Adv. Eng. Softw.*, 33(7-10):377–387.
- Giraldo FX, Hesthaven JS, Warburton T (2002) Nodal high-order discontinuous galerkin methods for the spherical shallow water equations. *Journal of Computational Physics*, 181:499 – 525.
- Heinze T, Hense A (2002) The shallow water equations on the sphere and their lagrange-galerkin-solution. *Meteorol. Atmos. Phys.*, 81:129–137.
- Hanert E, Le Roux DY, Legat V, Deleersnijder E (2004) Advection schemes for unstructured grid ocean modelling. *Ocean Modelling*, 7:39–58.
- Hanert E, Le Roux DY, Legat V, Deleersnijder E (2005) An efficient finite element method for the shallow water equations. *Ocean Modelling*, 10:115–136.
- Lockard DP, Atkins HL (1999) Efficient implementations of the quadrature-free discontinuous galerkin method. In *Proceeding of 14th AIAA CFD conference*. AIAA.
- Li X (2003) *Mesh Modification procedure for General 3-D Non-Manifold Domains*. PhD thesis, Renselear Polytechnic Indtitute.
- Luthar M, O’Brien JJ (1985) A model of the seasonal circulation in the arabian sea forced by observed winds. *Progr. Oceanogr.*,

14:353–385.

Li X, Remacle J-F, Chevaugéon N, Shephard MS (2004) Anisotropic mesh gradation control. In 13th International Meshing Roundtable.

Marchandise E, Chevaugéon N, Remacle J-F (2005) Spatial and spectral superconvergence of discontinuous galerkin methods applied to hyperbolic problems. *Journal of Computational and Applied Mathematics*,. Accepted for publication.

Naithani J, Deleersnijder E, Plisnier PD (2003) Analysis of wind-induced thermocline oscillations of lake tanganyika. *Environmental Fluid Mechanics*, 3:23–39.

Nair RD, Thomas SJ, Loft RD (2005) A discontinuous galerkin global shallow water model. *Monthly Weather Review*, 133:876–888.

Pietrzak J, Deleersnijder E, Schroeter J (Editors)(2005) The second international workshop on unstructured mesh numerical modelling of coastal, shelf and ocean flows (delft, the netherlands, september 23-25, 2003). *Ocean Modelling (special issue)*, 10:1–252.

Pain CC, Piggott MD, Goddard AJH, Fang F, Gorman GJ, Marshall DP, Eaton MD, Power PW, de Oliveira CRE (2005) Three-dimensional unstructured mesh ocean modelling. *Ocean Modelling*, 10:5–33.

Remacle J-F, Li X, Shephard MS, Flaherty JE (2005) Anisotropic adaptive simulation of transient flows using discontinuous galerkin methods. *International Journal for Numerical Methods in Engineering*, 62(7):899–923.

Roe PL (1981) Approximate riemann solvers, parameter vectors and difference schemes. *Journal of Computational Physics*, 43:357–372.

Remacle JF, Soares Frazão S, Li X, Shephard MS (2006) An adaptive discretization of shallow-water equations based on discontinuous galerkin methods. *International Journal for Numerical Methods in Fluids*, 52:903–923.

Speares W, Berzins M (1997) A 3d unstructured mesh adaptation algorithm for the time-dependent shock-dominated problems. *International Journal for Numerical Methods in Fluids*, 25(1):81–104.

Schwanenberg D, Kongeter J (2000) A discontinuous galerkin method for the shallow water equations with source terms. *Computational Science and Engineering*, 11:419–424.

Stommel H (1948) The westward intensification of wind-driven ocean currents. *Transactions - American Geophysical Union*, 29:202–206.

Soares Frazão S, Zech Y (2002) Dam-break in channels with 90-degree bend. *Journal of Hydraulic Engineering, American Society of Civil Engineers*, 128:956–968.

Soares Frazão S, Zech Y (2002) Undular bores and secondary waves - experiments and hybrid finite-volume modelling. *Journal of Hydraulic Research*, 40:33–34.

Vreugdenhill CB (1994) Numerical methods for shallow water flow. *Water Science and Technology Library. Kluwer Academic Publishers*.

Woodberry KE, Luthar ME, O'Brian JJ (1989) The wind-driven seasonal circulation in the southern tropical indian ocean. *J. Geophys. Res.*, 94:17,985–18,002.

List of Figures

1	Shallow water notations for water depth H with a time-independent bathymetry h . Notice that the relative elevation η is usually several orders of magnitude smaller than the unperturbed depth.	11
2	Local mesh modifications. Edge split (top), edge collapse (middle) and edge swap (bottom). The zone depicted in bold represents the cavity that is modified by the local mesh modification.	11
3	Mesh size fields and adaptive meshes obtained at different time steps, for the propagation of a typical anticyclonic eddy in the Gulf of Mexico (cf. section 4.2). The mesh on top includes 14545 triangles while the one on bottom includes 9618 triangles.	12
4	An element with its three surrounding neighbors.	12
5	Isolines of the stream function obtained for the Stommel model with the following parameters: $f_0 = 10^{-4} s^{-1}$, $\beta_0 = 2 \cdot 10^{-11} m^{-1} s^{-1}$, $\tau_0 = 10^{-1} Nm^{-2}$, $\gamma = 10^{-6} s^{-1}$, $g = 10 ms^{-2}$, $h = 10^3 m$, $\rho = 10^3 kgm^{-3}$ and $L_x = L_y = 10^6 m$ the length of the domain along the x and y dimensions.	13
6	Convergence of the L^2 norm of the error ϵ vs. the local mesh size h using (a) uniformly refined meshes and using (b) adaptively refined meshes.	13
7	The evolution of the maximum error, located in the western boundary layer for this Stommel model, showing the advantages of coupling both adaptivity and high order elements, which can be done in a simple and efficient way with the DG method.	14
8	The global and local effectivity index computed with first order elements both tend to one, indicating that the jumps can be considered as efficient error estimators.	14
9	The local effectivity fields present the same “boundary layer structure”	15
10	Notations for the shallow water reduced gravity model, with the time-independent height h and ξ the downward displacement of the interface between the two layers.	15
11	Isolines of elevation field and velocity norm, and the corresponding adaptive mesh, respectively, at different times of the eddy propagation. On each plot, the 40 iso- η lines extend from $-35 m$ (blue lines) to $65 m$ (red lines), while the 20 isovelocity lines extend from $0 m/s$ to $1.5 m/s$	16

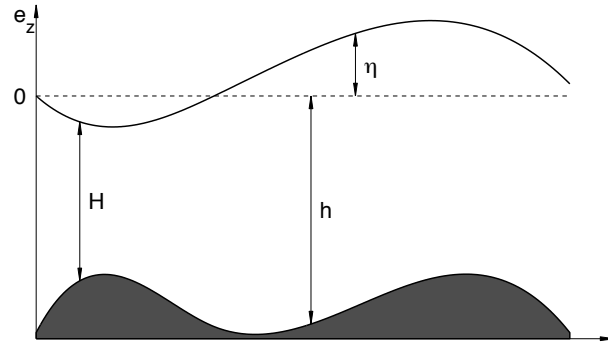


Fig. 1. Shallow water notations for water depth H with a time-independent bathymetry h . Notice that the relative elevation η is usually several orders of magnitude smaller than the unperturbed depth.

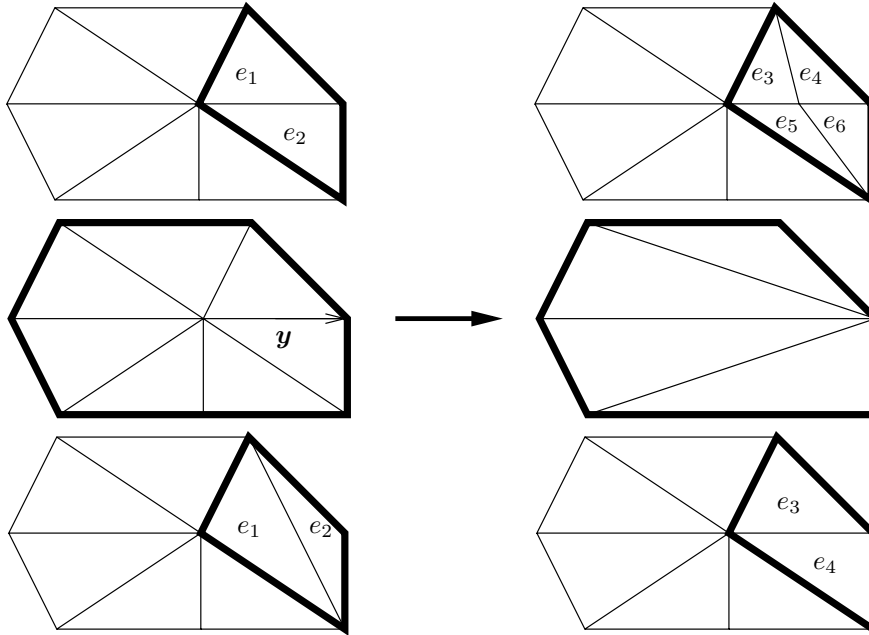


Fig. 2. Local mesh modifications. Edge split (top), edge collapse (middle) and edge swap (bottom). The zone depicted in bold represents the cavity that is modified by the local mesh modification.

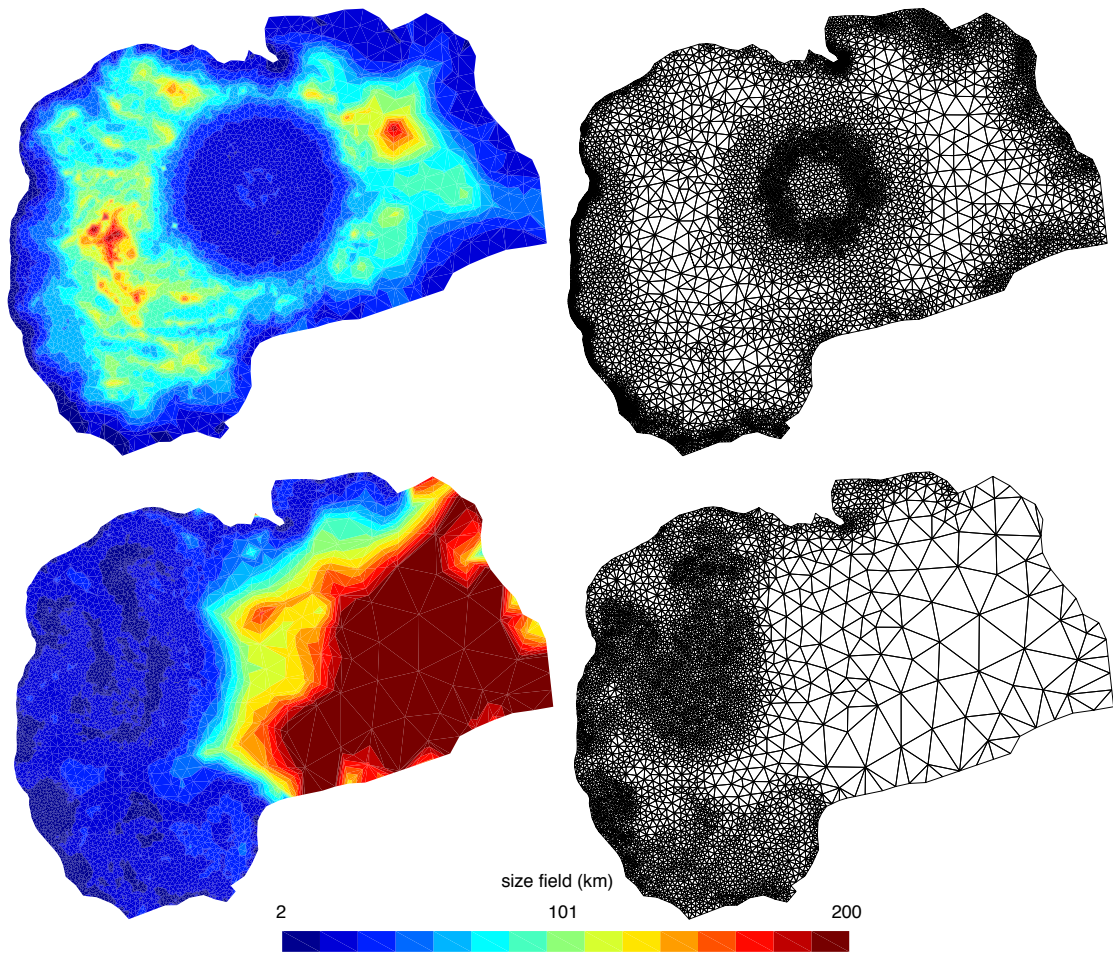


Fig. 3. Mesh size fields and adaptive meshes obtained at different time steps, for the propagation of a typical anticyclonic eddy in the Gulf of Mexico (cf. section 4.2). The mesh on top includes 14545 triangles while the one on bottom includes 9618 triangles.

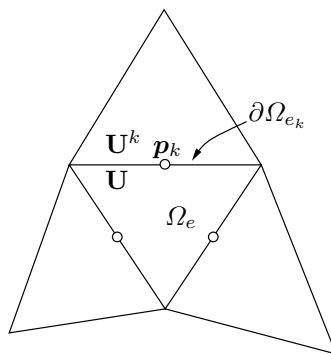


Fig. 4. An element with its three surrounding neighbors.

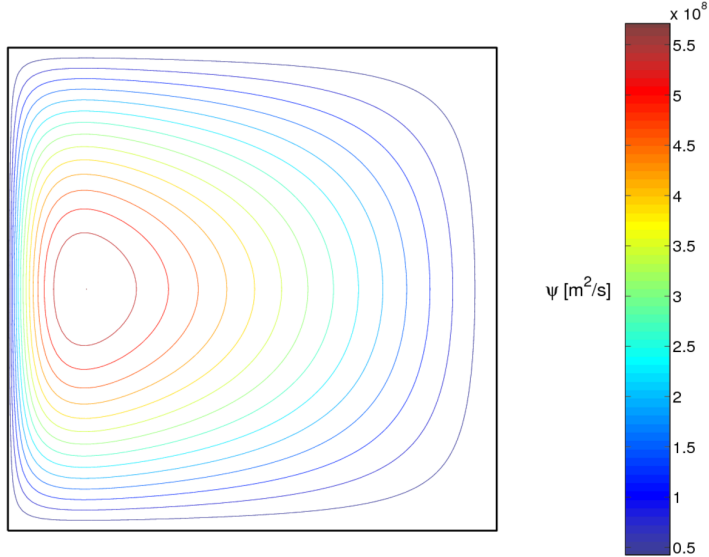
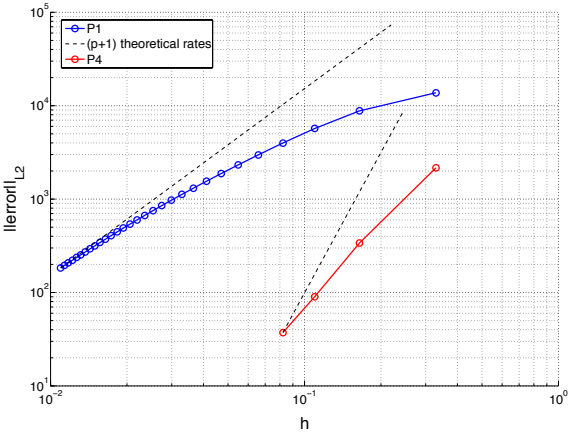
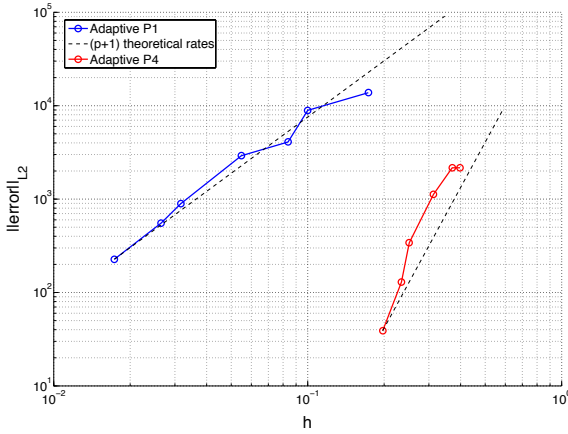


Fig. 5. Isolines of the stream function obtained for the Stommel model with the following parameters : $f_0 = 10^{-4} s^{-1}$, $\beta_0 = 2 \cdot 10^{-11} m^{-1}s^{-1}$, $\tau_0 = 10^{-1} Nm^{-2}$, $\gamma = 10^{-6} s^{-1}$, $g = 10 ms^{-2}$, $h = 10^3 m$, $\rho = 10^3 kgm^{-3}$ and $L_x = L_y = 10^6 m$ the length of the domain along the x and y dimensions.

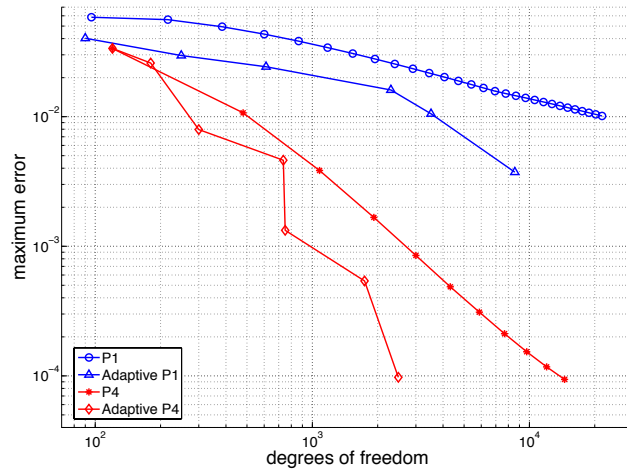


(a) structured mesh



(b) adaptive mesh

Fig. 6. Convergence of the L^2 norm of the error ϵ vs. the local mesh size h using (a) uniformly refined meshes and using (b) adaptively refined meshes.



(a) Evolution of the maximum error vs. degrees of freedom

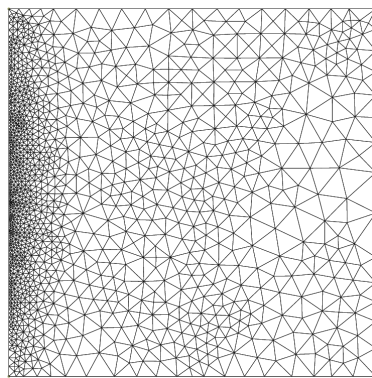
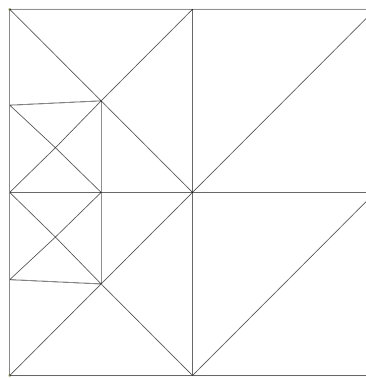
(b) 1st order adaptive mesh
 $e_{max} = 10^{-2}$ (c) 4th order adaptive mesh
 $e_{max} = 10^{-2}$

Fig. 7. The evolution of the maximum error, located in the western boundary layer for this Stommel model, showing the advantages of coupling both adaptivity and high order elements, which can be done in a simple and efficient way with the DG method.

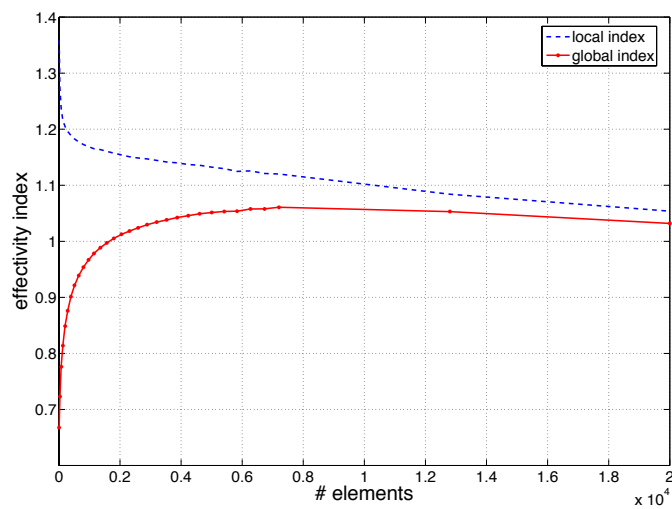


Fig. 8. The global and local effectivity index computed with first order elements both tend to one, indicating that the jumps can be considered as efficient error estimators.

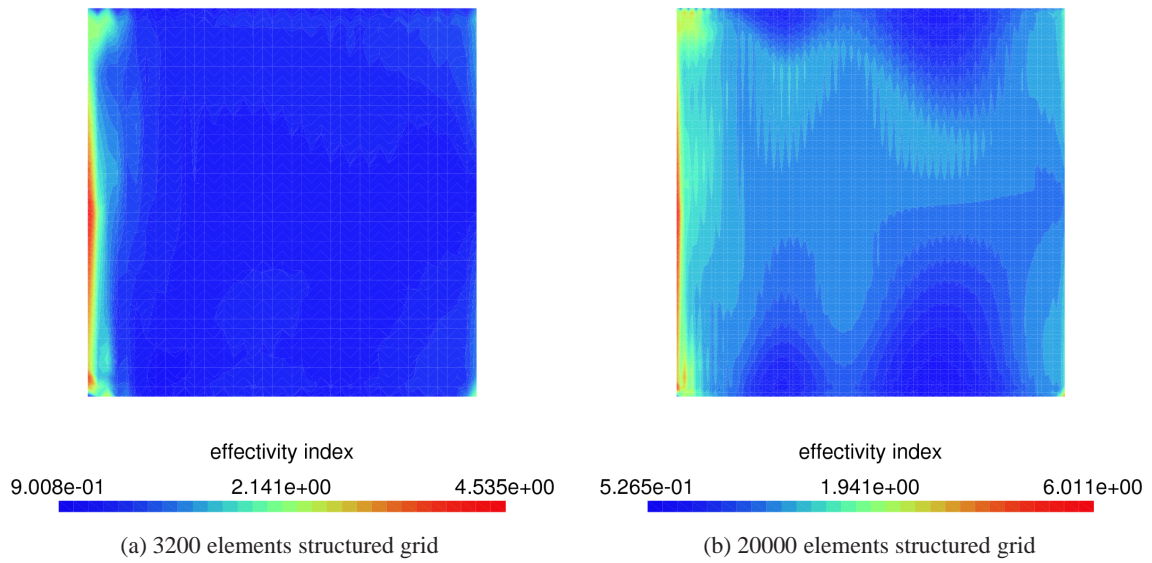


Fig. 9. The local effectivity fields present the same “boundary layer structure”

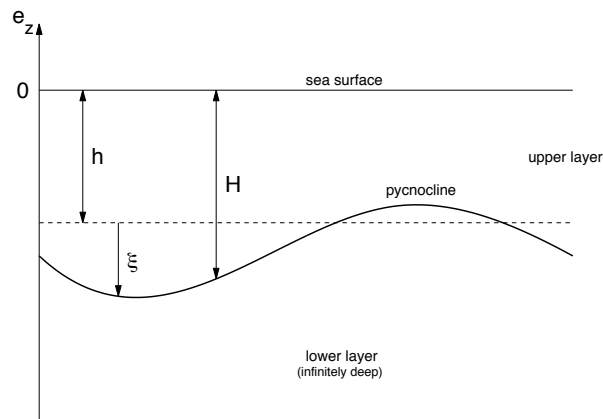


Fig. 10. Notations for the shallow water reduced gravity model, with the time-independant height h and ξ the downward displacement of the interface between the two layers.

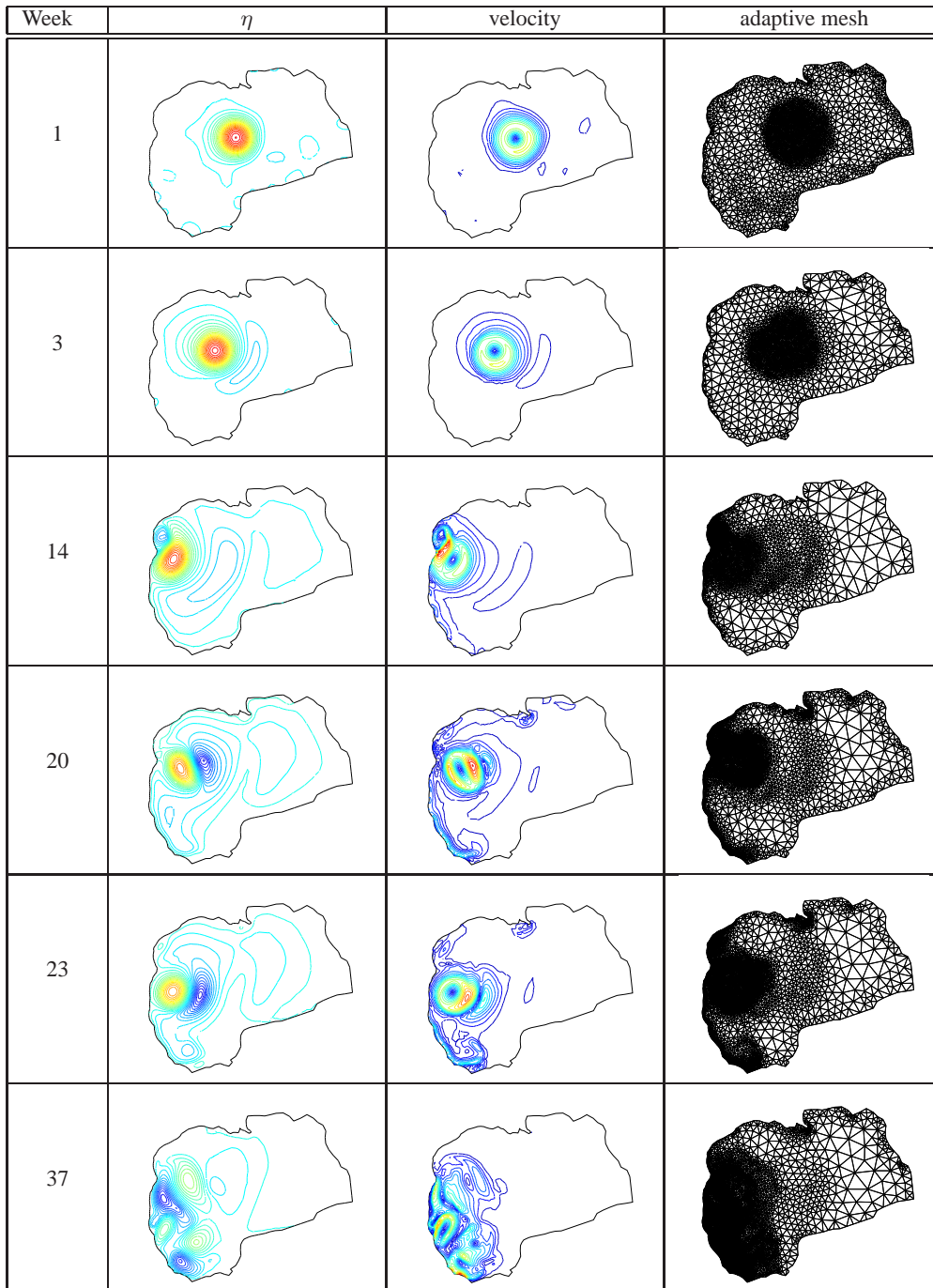


Fig. 11. Isolines of elevation field and velocity norm, and the corresponding adaptive mesh, respectively, at different times of the eddy propagation. On each plot, the 40 iso- η lines extend from -35 m (blue lines) to 65 m (red lines), while the 20 isovelocity lines extend from 0 m/s to 1.5 m/s.